

Human-induced changes to the global ocean water masses and their time of emergence

Article

Accepted Version

Silvy, Y., Guilyardi, E. ORCID: <https://orcid.org/0000-0002-2255-8625>, Sallée, J.-B. and Durack, P. J. (2020) Human-induced changes to the global ocean water masses and their time of emergence. *Nature Climate Change*, 10. pp. 1030-1036. ISSN 1758-678X doi: <https://doi.org/10.1038/s41558-020-0878-x> Available at <https://centaur.reading.ac.uk/92392/>

It is advisable to refer to the publisher's version if you intend to cite from the work. See [Guidance on citing](#).

To link to this article DOI: <http://dx.doi.org/10.1038/s41558-020-0878-x>

Publisher: Nature

All outputs in CentAUR are protected by Intellectual Property Rights law, including copyright law. Copyright and IPR is retained by the creators or other copyright holders. Terms and conditions for use of this material are defined in the [End User Agreement](#).

www.reading.ac.uk/centaur

CentAUR

Central Archive at the University of Reading

Reading's research outputs online

1
2
3
4
5
6
7
8
9
10
11
12
13
14
15
16
17
18
19

**Human-induced changes to the global ocean water-masses
and their time of emergence**

Yona Silvy^{1,*}, Eric Guilyardi^{1,2}, Jean-Baptiste Sallée¹ and Paul J. Durack³

*¹LOCEAN-IPSL, Laboratoire d'Océanographie et du Climat : Expérimentation et
Approches Numériques (Sorbonne Université/CNRS/IRD/MNHN), Paris, France*

²NCAS-Climate, University of Reading, UK

*³Program for Climate Model Diagnosis and Intercomparison, Lawrence Livermore
National Laboratory, Livermore, California, USA*

Corresponding author:

Yona Silvy (yona.silvy@locean-ipsl.upmc.fr)
LOCEAN-IPSL
Sorbonne Université, Boîte 100, 4 place Jussieu, 75252 Paris

20 **[Abstract]**

21 **The World Ocean is rapidly changing, with global and regional modification of**
22 **temperature and salinity, resulting in widespread and irreversible impacts. While**
23 **the most pronounced observed temperature and salinity changes are located in**
24 **the upper ocean, changes in water-masses at depth have been identified and will**
25 **likely strengthen in the future. Here, using 11 climate models, we define when**
26 **anthropogenic temperature and salinity changes are expected to emerge from**
27 **natural variability in the ocean interior along density surfaces. The models**
28 **predict that in 2020, 20–55% of the Atlantic, Pacific and Indian basins have an**
29 **emergent anthropogenic signal; reaching 40–65% in 2050, and 55–80% in 2080.**
30 **The well-ventilated Southern Ocean water-masses emerge very rapidly, as early**
31 **as the 1980s-1990s, while the Northern Hemisphere emerges in the 2010s-2030s.**
32 **Our results highlight the importance of maintaining and augmenting an ocean**
33 **observing system capable of detecting and monitoring persistent anthropogenic**
34 **changes.**

35 **[Main]**

36 Observed ocean temperature and salinity changes have been partially attributed to
37 human activities, with global ocean heat content change identified in the early 2000s^{1,2},
38 and temperature and salinity changes in the upper (0-700 m) and intermediate (700-
39 2000 m) ocean in more recent times³⁻¹¹. A few studies focused on more specific
40 regions, with detected human-induced changes to ocean salinity in the Tropical
41 Pacific⁹, the Atlantic¹⁰, and the Southern Ocean¹¹. However, there are still vast regions
42 of the World Ocean, particularly at depth, where anthropogenic change remains
43 undetected. The lack of positive attribution can be due to poor observational coverage,
44 weak changes, or because natural variability is large and is hiding forced changes.
45 Because of the slow transport of heat and salt in the ocean interior, some regions in the
46 deep ocean may be isolated from human-induced changes for a long time as the climate
47 signal propagates from the surface to the ocean interior. Other regions, which are more
48 directly connected to the surface by atmosphere-ocean exchanges, ocean circulation
49 and mixing, may respond more quickly. Based on anthropogenically-forced climate
50 model simulations it is possible to estimate where and when the human-induced signal
51 emerges against the natural background climate variability in the ocean interior.

52

53 While investigating the timescale of anthropogenic signal emergence in the climate
54 system, past studies have focused on surface temperature¹²⁻¹⁷, precipitation^{18,19}, sea
55 level rise²⁰ as well as marine ecosystem drivers and ocean carbon cycle indicators²¹⁻
56 ²⁶. It was shown that temperature and salinity are potentially good indicators for
57 detecting anthropogenic change in the next few decades²⁷. Here, we investigate for the
58 first time the emergence and associated probabilistic range of human-induced salinity
59 changes at depth, in basin-scale zonal means, using a multi-model framework. We

60 focus on the ocean interior below the “bowl”, i.e. below the deepest winter mixed layer
61 and we use climate models participating in the 5th phase of the coupled model
62 intercomparison project (CMIP5). Ocean circulation below the bowl primarily flows
63 along density surfaces. Density surfaces can move vertically (heave) for several
64 reasons including transient dynamical changes unrelated to atmosphere-forced and
65 ocean-ingested heat or freshwater changes, that manifest as temperature and salinity
66 changes when assessed on a given pressure level. In an endeavour to detect the earliest
67 time of emergence, we therefore remove from our analysis all signal associated to
68 transient dynamical change by investigating temperature and salinity changes on
69 neutral density levels (see Methods). On a density surface, changes of salinity and
70 temperature are by definition correlated, so to avoid redundancy we will hereafter only
71 discuss salinity changes.

72

73 Observed zonally-averaged salinity changes along density surfaces show remarkably
74 similar structures across different basins in the Southern Hemisphere (Figure 1a,
75 Supplementary Figure 1a)^{28,29}. These features include a subtropical freshening in the
76 upper 1000 metres in the density range of Subantarctic Mode and Intermediate Waters
77 ($26.5\text{-}27\text{ kg.m}^{-3}$), surrounded by a relatively strong salinity increase in the tropical
78 shallow cells and a slightly more moderate salinity increase in the range of Upper
79 Circumpolar Deep Waters ($\sim 50^{\circ}\text{S}\text{-}60^{\circ}\text{S}$, $\sim 27.5\text{ kg.m}^{-3}$). The Northern Hemisphere
80 Pacific presents a similar geographical salinification/freshening/salinification pattern
81 of change. The North Atlantic features a subpolar freshening extending into the
82 subtropics along the $27.7\text{-}28\text{ kg.m}^{-3}$ isopycnals as well as a freshening along the 27
83 kg.m^{-3} isopycnal from the subtropics to the equator and southward, capped by a strong
84 salinity increase in the upper ocean and smaller increase at depth. Strong salinification

85 is observed in the North Indian, spanning almost all density ranges and suggesting the
86 influence of marginal sea outflows of high salinity dominates.

87 These large-scale patterns of multi-decadal change have been proposed to be caused
88 by regional surface changes in freshwater fluxes²⁹⁻³² (wet regions get wetter and dry
89 regions get dryer), as well as from surface warming shifting isopycnal outcrops
90 poleward and along which the signal penetrates the ocean interior³⁰⁻³².

91

92 Although the amplitude of the change is weaker in the multi-model mean (MMM of
93 11 models; Figure 1b and Supplementary Figure 1b) than in the observation-based
94 estimate – which is expected for a multi-model ensemble mean as it washes out change
95 patterns of water-masses with slightly different geographies thus not exactly aligned –
96 the main patterns of change are reproduced. Indeed, the observed
97 salinification/freshening/salinification from equator to pole in the Southern
98 Hemisphere of all three basins and in the Northern Hemisphere Pacific is replicated in
99 the models, although we note the Mode Water freshening in the Southern Hemisphere
100 tends to appear on slightly lighter density classes in the models than in the observations
101 (around 26 kg.m^{-3} in the models versus $26.5\text{-}27 \text{ kg.m}^{-3}$ in the observations), consistent
102 with past studies^{11,31,33}. The magnitude of change within the individual model
103 ensembles is equivalent to observed estimates (Supplementary Figure 3) and the
104 change is robust across models in regions where the observed signal is the strongest,
105 indicative of a coherent forced change. The Northern Indian ocean shows a change
106 pattern of opposite sign in the MMM than in observations, as models have large
107 regional errors there. As the Durack & Wijffels 2010 (hereafter DW10) analysis ends
108 in 2008 (Figure 1a), we also compute the 1950-2017 change using the EN4³⁴
109 observation-based ocean reanalysis (Supplementary Figure 2a). The EN4 spatial

110 patterns of change are extremely similar to those of DW10, giving confidence in the
111 robustness of these identified observed patterns. In the MMM, the patterns of change
112 identified during the 1950-2008 period (Figure 1b and Supplementary Figure 1b)
113 become more robust when extending the period to 2017 and the amplitude of the
114 change increases (Supplementary Figure 2b).

115 To more quantitatively compare the observed and simulated trends in water-masses
116 regionally, a diagnostic of the trends in 9 regions of interest is shown (Figure 1c). In
117 both observations and models, these regions correspond to the salinity increase in the
118 subpolar Southern Ocean, the freshening in the Southern Hemisphere subtropics, the
119 increase (freshening) in the northern subtropical Atlantic (Pacific) and the increase in
120 the subpolar North Pacific. The coordinates are chosen to best capture these patterns
121 and tailored to the water-mass ranges of each model as those are not necessarily
122 reproduced at the same locations. Approximate boxes are shown in Figure 1a, and the
123 exact boxes can be found in Supplementary Figure 1a for the observations and
124 Supplementary Figure 4 for each model. We also run the same diagnostic for EN4.
125 Regional trends in the observational estimates and models (Figure 1c) are within the
126 same order of magnitude, although the DW10 values tend to lie systematically on the
127 higher end of the model distribution or even outside in some sections of the poorly-
128 sampled Southern Hemisphere, suggesting that the models might simulate a
129 conservative estimate of the change. In the well-sampled Northern Hemisphere, both
130 observational estimates fall within the model distribution. In all regions, EN4 yields a
131 smaller trend than DW10, consistent with the respective methods of these estimates
132 (in data-sparse regions, EN4 is restored towards the climatology, thus providing a very
133 conservative estimate of change). Overall, this gives us confidence in the ability of
134 models to reproduce these regional patterns of change.

135

136 Based on the same model suite, we now determine the “anthropogenic” component of
137 the change by subtracting from the salinity computed in the historical simulations, the
138 salinity computed in idealized coincident simulations where human-induced forcings
139 are removed (historicalNat). At the end of the 20th century it is striking that the
140 simulated historical change (Figure 1b) is very close to the estimated “anthropogenic”
141 contribution (Figure 2a), with a Pearson’s spatial correlation coefficient of 0.88,
142 suggesting that human-induced forcings are responsible for most of the observed
143 salinity change during the 2nd half of the 20th century^{5,9-11}. The pattern of the historical
144 anthropogenic signal is further amplified from 2006 and into the 21st century under a
145 high emission scenario (RCP8.5; Figure 2b), confirming the robustness of the
146 structures of the anthropogenic forced change over the observed time period. As this
147 signal appears qualitatively robust and human-induced, we now investigate when it
148 can be statistically unambiguously distinguished from natural background variability
149 over the 1861-2100 period (note that unlike previous studies, we use “natural” rather
150 than “unforced” variability, see Methods).

151

152 We define the time of emergence (ToE) of salinity change as the year when the
153 anthropogenic signal (ranging from 1861 to 2100) exceeds and never falls back below
154 twice the typical natural variability “noise” threshold (the interannual standard
155 deviation of the historicalNat experiment), such that emergence is detected within the
156 95% confidence interval (see Methods for details). We are choosing a rather high
157 estimate of the noise envelope (see Methods), thus possibly yielding conservative ToE
158 results. Nevertheless, early detection is found: in all regions that show a robust pattern
159 of change, the multi-model median ToE falls between the late 20th century and the first

160 decades of the 21st century (Figure 3a) and there is a noteworthy agreement between
161 models on the sign of the signal (see also inter-model spread in Supplementary Figure
162 5). Regions that do not emerge show no agreement between models (grey areas in
163 Figure 3a). In 2020, most of the identified forced patterns have already emerged in the
164 ocean interior, with 20-45% of the zonally averaged basin emerged in the Atlantic; 20-
165 55% in the Pacific and 25-50% in the Indian (Figure 3b, 1st-3rd quartiles). These
166 numbers rapidly increase, reaching 35-55% in the Atlantic in 2050 to 55-65% in 2080;
167 45-65% to 60-75% in the Pacific; 45-65% to 60-80% in the Indian.

168

169 The earliest ToE are found in the Southern Hemisphere subtropical (40-20°S) and
170 subpolar (60-40°S) areas, with a median ToE as early as the 1980s, and overall earlier
171 than 2020. The subtropical Southern Ocean is a dominant region for heat uptake
172 associated with the formation and subduction of water-masses ventilating the
173 subtropical gyres with Mode and Intermediate waters^{33,35}. The early emergence of the
174 human-induced signal in this region is consistent with the observed changes that have
175 been detected and attributed to anthropogenic forcings¹¹. Model agreement in the
176 southern subtropical Atlantic from 40–20°S is weak in the upper 1000 m, reflecting
177 that unlike the Indian and Pacific, this basin is not associated with a well ventilated
178 layer of Subantarctic Mode water³⁵. Instead, the upper 1000 m in the Southern Ocean
179 Atlantic basin is populated with newly ventilated Intermediate waters³⁵, whose
180 circulation and subduction are poorly represented by the CMIP5 model suite³³. The
181 model spread is relatively narrow for the Southern Hemisphere subtropics (2-3 decades
182 for the interquartile range in the Pacific and Indian sectors; Supplementary Figure 5),
183 and slightly larger for the subpolar Southern Ocean. We note that the emergence in the
184 subpolar Southern Ocean is to be assessed cautiously, with most models rapidly

185 limiting spurious open ocean deep convection due to near-surface freshening^{36,37},
186 therefore arguably warming at depth (1000-2000 m) much faster than in the real world
187 (in the subpolar Southern Ocean, deep convection acts to extract heat from the interior
188 ocean and release it to the atmosphere³⁸). The other regions featuring an emergence of
189 the signal in the first decades of the 21st century are the northern Pacific between 10-
190 30°N and 40°N-60°N, with a median ToE from the 2010s to 2040 and an inter-model
191 range of a few decades. The signal in the North Atlantic also emerges in the early
192 decades of the 21st century, mostly before 2020, with an interquartile range of two to
193 four decades. The inter-model range gives a measure of the uncertainty that the climate
194 models are providing, and so a spectrum of possibilities for the real world to lie within.
195 There is decadal to multi-decadal variability between realizations and between models,
196 as well as model errors, which means it is difficult to get that range below O(10 years).
197
198 Because each model can represent a given water-mass at slightly different latitude or
199 density, we again delineate model-specific water-mass ranges that are uniquely
200 defined for each model, so a clearer, quantitative water-mass centric model
201 intercomparison can be performed (same regions as Figure 1c; see approximate
202 regions in Figure 2b and exact boxes for each model in Supplementary Figure 4 in
203 original density space). Additionally, and again to increase the signal to noise ratio,
204 because each model can have a different climate sensitivity for a given forcing
205 scenario, here we associate, for each model member, the ToE of the anthropogenic
206 signal in all 9 regions to the corresponding global mean surface warming at that time
207 under the RCP8.5 scenario (global mean surface air temperature (GSAT) increase
208 relative to the pre-industrial era, Figure 4). Supplementary Figure 6 shows the same
209 analysis, as a function of time (ToE axis instead of GSAT anomaly).

210 Most models predict that salinity change signals emerge between +0.5°C and +2°C of
211 global mean surface warming, corresponding to a ToE between the late 20th century
212 and the first decades of the 21st century (Figure 4). According to this distribution, there
213 is a 100% probability for the anthropogenic signal in the Northern subpolar Pacific and
214 in the Southern Hemisphere Pacific and Indian subtropics to emerge before a +2°C
215 warming, and over 75% probability to emerge before +1.5°C – and even before +1°C
216 for the Pacific southern subtropics (note observed global mean surface warming to
217 2018 is about 1°C³⁹). The subpolar Southern Ocean sectors have a relatively early
218 median emergence (~0.8°C-1.3°C), but a wide model spread, especially in the Pacific,
219 probably reflecting model deficiencies in representing this part of the ocean^{36,37}. The
220 Northern Hemisphere subtropical water-masses emerge slightly later than their
221 Southern Hemisphere counterparts (except in the Atlantic basin), with about 75%
222 probability to emerge before +2.25°C. We expect the dependence of these results to
223 slower warming scenarios (different RCPs) to be limited, as most models present a
224 signal emerging before there is a significant difference between scenarios (see
225 comparison of the RCP4.5 and RCP8.5 warming in Supplementary Figure 7).

226

227 We repeat the same analysis on an idealized emission scenario where CO₂
228 concentration in the atmosphere increases by 1% every year (1pctCO₂), i.e. a much
229 faster forcing than observed in the 20th century or projected for the 21st century (see
230 Supplementary Figures 6 and 8, and CO₂ signal patterns in Supplementary Figure 9).
231 The overall agreement in the emergence of a climate signal in different water-masses
232 across the different models and the two types of very different timing of forcing
233 scenarios (RCP8.5, 1pctCO₂) offers confidence in simulated emergence patterns and
234 confirms the dominant role of CO₂ emissions.

235

236 In analysing emergence timescales in the climate system, previous studies^{20,21} showed
237 that spatial patterns of ToE are strongly determined by the unforced variability,
238 meaning that an earlier ToE arises in regions of weaker noise and vice-versa. We
239 investigate whether this is the case by examining the relative contributions of signal
240 and noise to the ToE regional pattern for each model, as well as the regional inter-
241 model spread (see Supplementary Discussion and Supplementary Figures 12 and 13).
242 We find that the time-independent noise level is not sufficient to explain the ToE
243 spread, which seems predominantly explained by the signal across regions and models,
244 i.e. either its strength, or its decadal to multi-decadal variability. This suggests that the
245 low noise level of the ocean interior makes it a unique place for early detection of
246 human-induced changes, even with the conservative estimate used here. Indeed,
247 although the anthropogenic climate signal might appear at the surface first, strong
248 background variability there can delay its emergence and counter-intuitively earlier
249 emergence can be found in the ocean interior, with geographical differences compared
250 to the surface. Surface air temperature and sea surface temperature in the RCP8.5
251 scenario were found to emerge mainly within the early to mid 21st century, showing
252 strong regional differences with earlier emergence in the tropics due to the low noise
253 level there than at higher latitudes^{14,15,20}. ToE is especially late in the Southern Ocean
254 for surface temperature, whereas we find the earliest emergence in this part of the
255 world under the surface. Half of the ocean area is expected to have emergent
256 thermosteric sea level rise in the 2040s, and when including additional effects such as
257 ice mass loss, as early as 2020²⁰. It is interesting to see that the timing of emergence
258 of changing patterns occurs differently for different variables, probably a testimony of
259 their distinctive interactions and feedbacks in the Earth system. This is clearly

260 illustrated by the very different patterns and timing of emergence of the change in the
261 different components of the ocean carbon cycle²⁶. The diversity of climate variables
262 investigated collectively provides a comprehensive understanding of the time of
263 emergence of the human-induced change in the Earth System, into which this study is
264 contributing additional insight.

265

266 This work suggests that a large portion of the observed change patterns in the ocean
267 interior is human-induced and will continue to respond to CO₂ emissions. If these
268 patterns have been suggested to be primarily driven by an increased surface warming
269 and water-cycle amplification^{29,31} (two processes that directly affect heat and salt in
270 the ocean thus density and circulation), understanding how these patterns will continue
271 to amplify in the future in a more stratified upper ocean⁴⁰ and with possibly modified
272 ocean circulation and mixing requires further investigation. In particular deciphering
273 which of the changing surface fluxes is likely to play a larger role, where and on what
274 timescales, can be for example explored with model-specific FAFMIP-like^{41,42}
275 mechanistic studies.

276 The Hemispheric asymmetry in emergence, with earlier ToEs in the Southern
277 Hemisphere subtropics is reminiscent of a number of recent studies stressing the
278 importance of the Southern Ocean for ocean heat and carbon storage, associated with
279 the overturning circulation⁴³⁻⁴⁵. It is noteworthy that this part of the world is
280 historically the most poorly sampled, and therefore the worst positioned for detecting
281 a forced climate signal in observations^{46,47}. The global pattern of human-induced
282 fingerprint of ocean interior change can be used to guide the future development of a
283 targeted global ocean observing system focused at monitoring and detecting future
284 ocean change. The maintenance of this observing system along with continued

285 investment in climate and ocean model development and evaluation, will provide the
286 necessary measurements and model tools to best inform adaptation and mitigation
287 strategies and policies going forward.

288

289

290 **[Methods]**

291 **Density binning of CMIP5 simulations**

292 In this study, we use a suite of CMIP5 climate models binned into a neutral density
293 framework, using the McDougall and Jackett (2005)⁴⁸ routine, to examine
294 anthropogenic signal in the ocean on approximated neutral surfaces (γ^a) compared with
295 natural climate variability. Zonal means are computed for each oceanic basin along
296 neutral density surfaces, which allows for a more water mass-centric assessment than
297 is possible using a standard pressure level analysis. We note that some vertical
298 movement (heave) of density surfaces can be due to climate change^{49,50}, but we don't
299 investigate those here. In addition to providing a cleaner signal and reducing the noise,
300 the density framework provides several other benefits, including a view of the ocean
301 interior delineated by its water-masses, useful for intermodel comparison^{33,51}, as water-
302 masses can be defined by their density range. Additionally, along density surfaces,
303 salinity and temperature changes compensate and thus have the same structure and
304 sign, and consequently the same emergence timescale.

305 To allow for a simpler and more intuitive visual representation, zonally-averaged
306 values are then remapped back to a pseudo-depth coordinate using a γ^a to pressure
307 relationship derived from observation-based product EN4³⁴ by a surface-to-bottom
308 mapping of the ocean per density layer. Note that all remapping of this paper,
309 irrespective of whether we are in the context of past, contemporary, or future, is done

310 with the exact same γ^a to pressure relationship which is based on contemporary
311 observations. The remapping is purely a visual tool here, which does not introduce any
312 signal: all signal, noise and ToE computations are done in γ^a space. All the data is
313 trimmed at the bowl (i.e. below the winter mixed layer depth), indicated by a dark grey
314 shading in the figures.

315

316 **ToE definition**

317 The ToE is computed both locally (for each grid point; Figure 3) and regionally in a
318 number of determined regions, using a manual fingerprint (i.e. regional model-specific
319 boxes fixed in time) to track the signal (Figure 4). We use an ensemble of 11 models
320 with a total of 35 realizations for the anthropogenic ToE, and 13 single-member
321 models for the CO₂ ToE (see Supplementary Table 1). The ToE is computed for each
322 individual member, then inter-member medians are derived, yielding a multi-model
323 distribution with the same weight for each model, and thus an estimate of the
324 uncertainty.

325 The anthropogenic signal is 240 years long, ranging from 1861 to 2100. It is defined
326 over the historical period (1861-2005) at each yearly time step as the salinity difference
327 between the historical experiment (fully-forced) and the time averaged historicalNat
328 value (natural forcings only: solar fluctuations and volcanic eruptions); and defined
329 over the projection period (2006-2100) at each yearly time step by the salinity change
330 between the RCP8.5 scenario (“business as usual”) and the time averaged historicalNat
331 value (same baseline for both periods to insure continuity). For each
332 historical+RCP8.5 ensemble member, the historicalNat time series used as the baseline
333 of the signal is the ensemble mean.

334 We note that the correct term for the signal defined above should be “externally
335 forced” as the influence of external natural forcings can be present during the historical
336 period; however, considering the greater influence of human-induced forcings over
337 time and especially in the ocean interior, we therefore refer to this signal as
338 “anthropogenic”. The possible influence of external natural forcings in the signal
339 during the historical period will occur in terms of additional decadal to multidecadal
340 variability.

341 The noise represents the bounds of background climate variability, and is built from
342 the interannual standard deviation of the historicalNat experiment (1861-2005, over
343 145 years). Within several historical+RCP8.5 members of a model, the noise is the
344 same and is defined using the maximum standard deviation of all available
345 historicalNat realizations within that model. The threshold of signal exceedance over
346 noise is chosen at two based on the large consensus in existing literature, and because
347 it represents a 95% confidence of signal emergence, but sensitivity to this threshold is
348 discussed in the Supplementary Materials (see Supplementary Figure 10). Overall, this
349 definition makes it a rather high (thus conservative) estimate of the noise envelope
350 (interannual noise, historicalNat choice instead of a pre-industrial control, two
351 standard deviations as the threshold and picking the maximum among historicalNat
352 members). The signal is considered to have emerged if it definitively exceeds the noise
353 threshold at least 20 years before the end of the projection to account for potential
354 “false” emergence - i.e. if the signal were to go back within the bounds of climate
355 variability afterwards^{20,52}. Note that some internal variability (and natural variability
356 over the historical period due to volcanic and sun forcings) remains in our signal
357 definition, which is not exactly the purely forced response to anthropogenic forcings

358 such as can be identified with the multi-model mean of a large ensemble, but is rather
359 a change and thus more similar to what real observational time series would look like.
360 The historicalNat experiment is a coherent choice for estimating natural climate
361 variability as it accounts for internal variability as well as external natural forcings,
362 both included in the forced experiments. However, we do test how our results are
363 affected by using the pre-industrial control (no external forcings) instead of the
364 historicalNat experiment in defining the noise, as is often done, and do not find the
365 time of emergence distributions to be much altered (see Supplementary Figure 11).
366 The change driven by the CO₂ forcing alone can be estimated in a similar way, by
367 taking the salinity difference between the yearly idealized 1pctCO₂ experiment (140
368 years) and the mean value of the pre-industrial control. The noise for CO₂ ToE is then
369 defined as the standard deviation of the pre-industrial control over the last 240 years
370 (as to have the same noise definition as done in Supplementary Figure 11 for the
371 turquoise boxes).

372

373 **ToE distribution of basin zonal means**

374 The gridpoint-per-gridpoint ToE distribution is calculated based on Lyu et al.'s
375 (2014)²⁰ methodology. A signal is considered to have emerged if its ToE is at least 20
376 years earlier than the end of the time series (2080 for the RCP8.5, 120 for the
377 1pctCO₂). At each gridpoint, the signal of each model realization can emerge with
378 either a positive (salinity increase) or negative (freshening) change, or not emerge at
379 all and stay within the bounds of climate variability. The distribution can be calculated
380 if at least half of the runs emerge with the same sign of the signal, or at least half of
381 the runs show no emergence, and if the outliers that have a different direction of change
382 are less than 5 (5 for the anthropogenic signal, 1 for the pure CO₂). We then compute

383 the distribution by excluding the outliers, first by computing the inter-member
384 medians, then the multi-model distribution using these medians so as to give each
385 model the same weight. If the conditions are not met, the location is labelled as “no
386 agreement”. See Lyu et al. (2014) supplementary material for details and examples.

387

388 **Manual fingerprint**

389 The regional ToEs are calculated by averaging both signal and noise in selected regions
390 (see Figure 2b). Namely, we defined: the Southern Ocean subpolar range,
391 encompassing signal associated with Upper Circumpolar Deep Water (around 40–
392 60°S; 27-28 kg.m-3); the Southern Ocean subtropical range, encompassing signal
393 associated with Mode and Intermediate Waters (around 20–40°S; 25-26.5 kg.m-3); the
394 Northern Hemisphere subtropical range, encompassing signal associated with Atlantic
395 and Pacific Mode Waters (around 20–40°N; 25-26 kg.m-3 in the Pacific; 26-27 kg.m-
396 3 in the Atlantic), and the Subpolar North Pacific, encompassing signal associated with
397 the North Pacific Intermediate Waters (around 40-60°N; 26-27 kg.m-3). The boxed
398 coordinates are model-specific, and were fixed (in γ^a space) based on the zonally-
399 averaged spatial pattern of the signal at the end of the time series (see Supplementary
400 Figure 4). The regional emergence of the signal (Figure 4) is based on a manual
401 fingerprint for each region displayed, thus slightly sensitive to the precise boxes used.
402 The patterns of change that already exist in the historical forced simulations continue
403 to exist in the same locations and enhance in the 21st century simulations, giving us
404 confidence in using boxes fixed in time.

405

406

407

408 **Warming scale**

409 Global surface warming at emergence was computed by taking each run's GSAT
410 (historical+RCP8.5) smoothed with a 10-year running mean, at the time of emergence
411 in each region. GSAT anomaly is calculated relative to the 1850-1900 period. The
412 same was done for the 1pctCO2 GSAT (Supplementary Figure 8).

413

414 **Percentage of basin emergence**

415 We define the percentage of emerged area in basin zonal means and under the surface
416 bowl at each time step by computing the cumulative sum over each basin of the number
417 of grid cells that have emerged before that time step, weighted by the thickness of their
418 respective density layer; and dividing it by the cumulative sum of each grid cell's
419 isopycnal thickness of that same basin zonal mean. The result is given in terms of area
420 as the latitudinal grid is regular with a 1° resolution (all models were interpolated on
421 that same horizontal regular grid). This is done for every model simulation, then the
422 inter-member medians are computed. Shown in Figure 3b are the median, 1st and 3rd
423 quartiles of the multi-model distribution.

424

425

426

427

428

429

430

431

432

433 **[Acknowledgments]**

434 We wish to thank Casimir de Lavergne, Alexey Fedorov, Peter Gleckler, Jonathan
435 Gregory, Ed Hawkins, Gurvan Madec, Herlé Mercier, Juliette Mignot, Ben Santer and
436 Laurent Terray for helpful discussions. We acknowledge the support from the “Make Our
437 Planet Great Again” project ARCHANGE (Agence Nationale pour la Recherche project
438 ANR-18-MPGA-0001), from the European Research Council (ERC) under the European
439 Union’s Horizon 2020 research and innovation program (grant agreement 637770) and
440 from the Centre National de la Recherche Scientifique. We also acknowledge the CMIP5
441 modelling groups, the ESGF and IPSL/ESPRI-MOD data distribution systems. The work
442 of PJD was prepared by Lawrence Livermore National Laboratory (LLNL) under
443 Contract DE-AC52-07NA27344 and is a contribution to the U.S. Department of Energy,
444 Office of Science, Climate and Environmental Sciences Division, Regional and Global
445 Modeling and Analysis Program. LLNL Release number: LLNL-JRNL-794900.

446

447

448

449

450

451

452

453

454

455

456

457

458 **[References]**

- 459 1. Barnett, T. P., Pierce, D. W. & Schnur, R. Detection of Anthropogenic Climate
460 Change in the World's Oceans. *Science* **292**, 270–274 (2001).
- 461 2. Reichert, B. K., Schnur, R. & Bengtsson, L. Global ocean warming tied to
462 anthropogenic forcing. *Geophys. Res. Lett.* **29**, 20-1-20-4 (2002).
- 463 3. Barnett, T. P. *et al.* Penetration of Human-Induced Warming into the World's
464 Oceans. *Science* **309**, 284–287 (2005).
- 465 4. Palmer, M. D., Good, S. A., Haines, K., Rayner, N. A. & Stott, P. A. A new
466 perspective on warming of the global oceans. *Geophys. Res. Lett.* **36**, (2009).
- 467 5. Pierce, D. W., Gleckler, P. J., Barnett, T. P., Santer, B. D. & Durack, P. J. The
468 fingerprint of human-induced changes in the ocean's salinity and temperature fields.
469 *Geophys. Res. Lett.* **39**, (2012).
- 470 6. Gleckler, P. J. *et al.* Human-induced global ocean warming on multidecadal
471 timescales. *Nat. Clim. Change* **2**, 524–529 (2012).
- 472 7. Tokarska, K. B., Hegerl, G. C., Schurer, A. P., Ribes, A. & Fasullo, J. T.
473 Quantifying human contributions to past and future ocean warming and thermosteric sea
474 level rise. *Environ. Res. Lett.* **14**, 074020 (2019).
- 475 8. Bilbao, R. A. F., Gregory, J. M., Bouttes, N., Palmer, M. D. & Stott, P.
476 Attribution of ocean temperature change to anthropogenic and natural forcings using the
477 temporal, vertical and geographical structure. *Clim. Dyn.* (2019) doi:10.1007/s00382-
478 019-04910-1.
- 479 9. Terray, L. *et al.* Near-Surface Salinity as Nature's Rain Gauge to Detect Human
480 Influence on the Tropical Water Cycle. *J. Clim.* **25**, 958–977 (2012).
- 481 10. Stott, P. A., Sutton, R. T. & Smith, D. M. Detection and attribution of Atlantic
482 salinity changes. *Geophys. Res. Lett.* **35**, (2008).
- 483 11. Swart, N. C., Gille, S. T., Fyfe, J. C. & Gillett, N. P. Recent Southern Ocean
484 warming and freshening driven by greenhouse gas emissions and ozone depletion. *Nat.*
485 *Geosci.* **11**, 836+ (2018).
- 486 12. Mahlstein, I., Knutti, R., Solomon, S. & Portmann, R. W. Early onset of
487 significant local warming in low latitude countries. *Environ. Res. Lett.* **6**, 034009
488 (2011).
- 489 13. Diffenbaugh, N. S. & Scherer, M. Observational and model evidence of global
490 emergence of permanent, unprecedented heat in the 20th and 21st centuries. *Clim.*

- 491 *Change* **107**, 615–624 (2011).
- 492 14. Hawkins, E. & Sutton, R. Time of emergence of climate signals. *Geophys. Res.*
493 *Lett.* **39**, n/a-n/a (2012).
- 494 15. Mora, C. *et al.* The projected timing of climate departure from recent variability.
495 *Nature* **502**, 183–187 (2013).
- 496 16. Diffenbaugh, N. S. & Charland, A. Probability of emergence of novel
497 temperature regimes at different levels of cumulative carbon emissions. *Front. Ecol.*
498 *Environ.* **14**, 418–423 (2016).
- 499 17. Lehner, F., Deser, C. & Terray, L. Toward a New Estimate of “Time of
500 Emergence” of Anthropogenic Warming: Insights from Dynamical Adjustment and a
501 Large Initial-Condition Model Ensemble. *J. Clim.* **30**, 7739–7756 (2017).
- 502 18. Giorgi, F. & Bi, X. Time of emergence (TOE) of GHG-forced precipitation
503 change hot-spots. *Geophys. Res. Lett.* **36**, (2009).
- 504 19. Mahlstein, I., Portmann, R. W., Daniel, J. S., Solomon, S. & Knutti, R.
505 Perceptible changes in regional precipitation in a future climate. *Geophys. Res. Lett.* **39**,
506 (2012).
- 507 20. Lyu, K., Zhang, X., Church, J. A., Slangen, A. B. A. & Hu, J. Time of
508 emergence for regional sea-level change. *Nat. Clim. Change* **4**, (2014).
- 509 21. Keller, K. M., Joos, F. & Raible, C. C. Time of emergence of trends in ocean
510 biogeochemistry. *Biogeosciences* **11**, 3647–3659 (2014).
- 511 22. Rodgers, K. B., Lin, J. & Frölicher, T. L. Emergence of multiple ocean
512 ecosystem drivers in a large ensemble suite with an Earth system model. *Biogeosciences*
513 **12**, 3301–3320 (2015).
- 514 23. Frölicher, T. L., Rodgers, K. B., Stock, C. A. & Cheung, W. W. L. Sources of
515 uncertainties in 21st century projections of potential ocean ecosystem stressors. *Glob.*
516 *Biogeochem. Cycles* **30**, 1224–1243 (2016).
- 517 24. Henson, S. A. *et al.* Rapid emergence of climate change in environmental
518 drivers of marine ecosystems. *Nat. Commun.* **8**, 14682 (2017).
- 519 25. Turk, D. *et al.* Time of Emergence of Surface Ocean Carbon Dioxide Trends in
520 the North American Coastal Margins in Support of Ocean Acidification Observing
521 System Design. *Front. Mar. Sci.* **6**, (2019).
- 522 26. Schlunegger, S. *et al.* Emergence of anthropogenic signals in the ocean carbon
523 cycle. *Nat. Clim. Change* 1–7 (2019) doi:10.1038/s41558-019-0553-2.
- 524 27. Banks, H. & Wood, R. Where to Look for Anthropogenic Climate Change in the

525 Ocean. *J. Clim.* **15**, 879–891 (2002).

526 28. Helm, K. P., Bindoff, N. L. & Church, J. A. Changes in the global hydrological-
527 cycle inferred from ocean salinity. *Geophys. Res. Lett.* **37**, (2010).

528 29. Durack, P. J. & Wijffels, S. E. Fifty-Year Trends in Global Ocean Salinities and
529 Their Relationship to Broad-Scale Warming. *J. Clim.* **23**, 4342–4362 (2010).

530 30. Durack, P. J., Wijffels, S. E. & Matear, R. J. Ocean Salinities Reveal Strong
531 Global Water Cycle Intensification During 1950 to 2000. *Science* **336**, 455–458 (2012).

532 31. Lago, V. *et al.* Simulating the Role of Surface Forcing on Observed
533 Multidecadal Upper-Ocean Salinity Changes. *J. Clim.* **29**, 5575–5588 (2016).

534 32. Zika, J. D. *et al.* Improved estimates of water cycle change from ocean salinity:
535 the key role of ocean warming. *Environ. Res. Lett.* **13**, 074036 (2018).

536 33. Sallee, J.-B. *et al.* Assessment of Southern Ocean water mass circulation and
537 characteristics in CMIP5 models: Historical bias and forcing response. *J. Geophys.*
538 *Res.-Oceans* **118**, 1830–1844 (2013).

539 34. Good, S. A., Martin, M. J. & Rayner, N. A. EN4: Quality controlled ocean
540 temperature and salinity profiles and monthly objective analyses with uncertainty
541 estimates: THE EN4 DATA SET. *J. Geophys. Res. Oceans* **118**, 6704–6716 (2013).

542 35. Sallée, J.-B., Speer, K., Rintoul, S. & Wijffels, S. Southern Ocean Thermocline
543 Ventilation. *J. Phys. Oceanogr.* **40**, 509–529 (2010).

544 36. de Lavergne, C., Palter, J. B., Galbraith, E. D., Bernardello, R. & Marinov, I.
545 Cessation of deep convection in the open Southern Ocean under anthropogenic climate
546 change. *Nat. Clim. Change* **4**, 278–282 (2014).

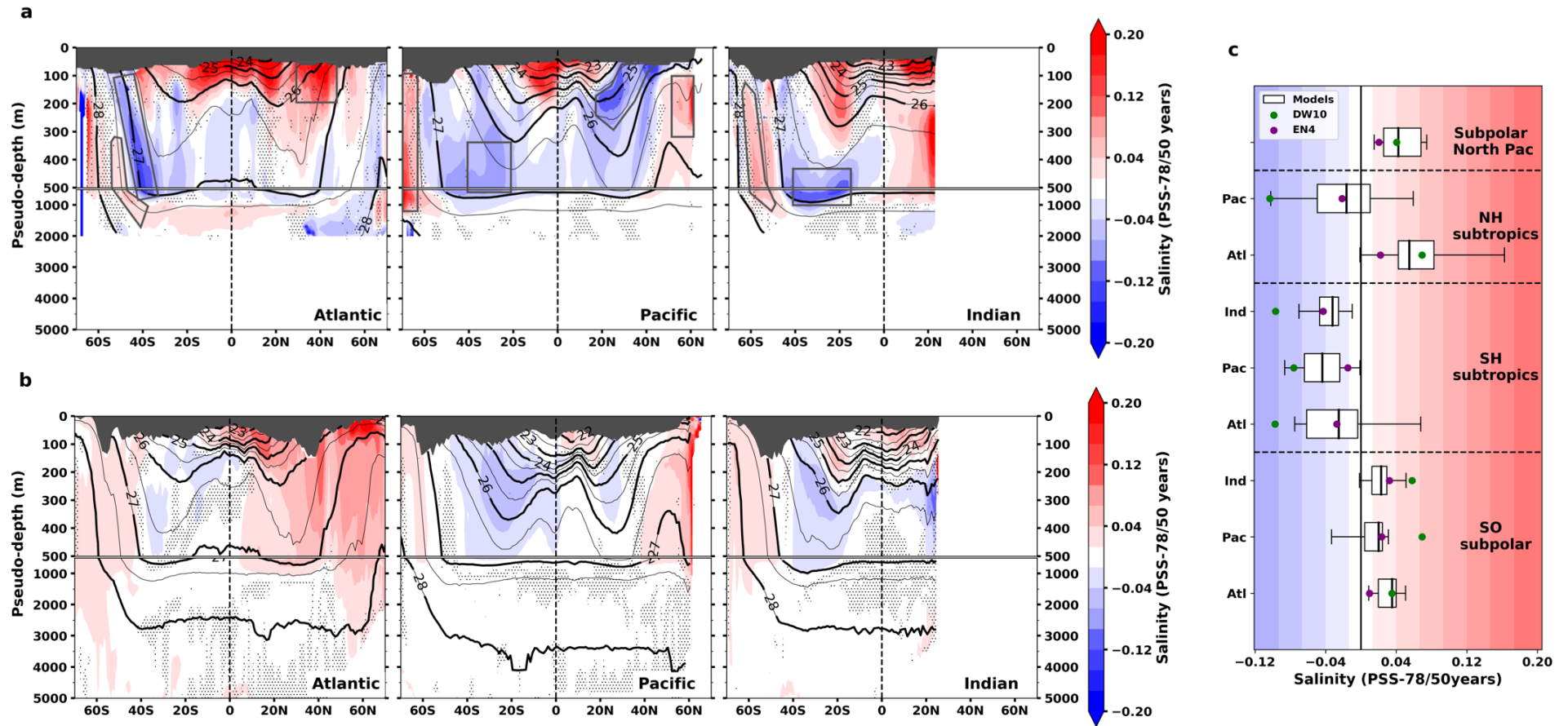
547 37. Heuzé, C., Ridley, J. K., Calvert, D., Stevens, D. P. & Heywood, K. J.
548 Increasing vertical mixing to reduce Southern Ocean deep convection in NEMO3.4.
549 *Geosci. Model Dev.* **8**, 3119–3130 (2015).

550 38. Dufour, C. O. *et al.* Preconditioning of the Weddell Sea Polynya by the Ocean
551 Mesoscale and Dense Water Overflows. *J. Clim.* **30**, 7719–7737 (2017).

552 39. Intergovernmental Panel on Climate Change. Summary for Policymakers. in
553 *Global warming of 1.5°C. An IPCC Special Report on the impacts of global warming of*
554 *1.5°C above pre-industrial levels and related global greenhouse gas emission*
555 *pathways, in the context of strengthening the global response to the threat of climate*
556 *change, sustainable development, and efforts to eradicate poverty* (2018).

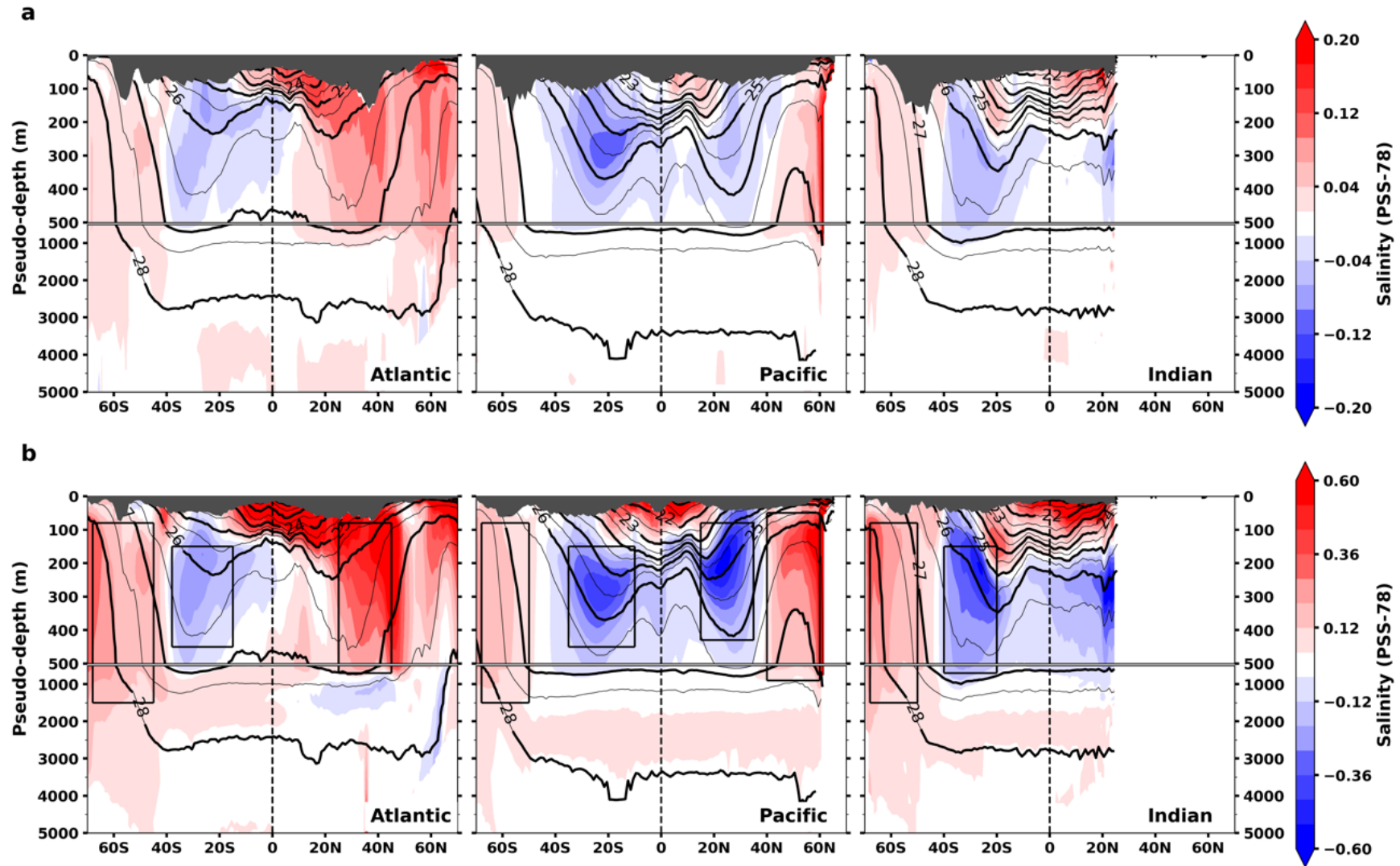
557 40. Yamaguchi, R. & Suga, T. Trend and Variability in Global Upper-Ocean
558 Stratification Since the 1960s. *J. Geophys. Res. Oceans* **124**, 8933–8948 (2019).

- 559 41. Gregory, J. M. *et al.* The Flux-Anomaly-Forced Model Intercomparison Project
560 (FAFMIP) contribution to CMIP6: investigation of sea-level and ocean climate change
561 in response to CO₂ forcing. *27* (2016).
- 562 42. Todd, A. *et al.* Ocean-only FAFMIP: Understanding Regional Patterns of Ocean
563 Heat Content and Dynamic Sea Level Change. (2020).
- 564 43. Gille, S. T. Decadal-Scale Temperature Trends in the Southern Hemisphere
565 Ocean. *J. Clim.* **21**, 4749–4765 (2008).
- 566 44. Khatiwala, S. P. *et al.* Global ocean storage of anthropogenic carbon.
567 *Biogeosciences* **10**, 2169–2191 (2013).
- 568 45. Frölicher, T. L. *et al.* Dominance of the Southern Ocean in Anthropogenic
569 Carbon and Heat Uptake in CMIP5 Models. *J. Clim.* **28**, 862–886 (2015).
- 570 46. Roemmich, D. *et al.* Unabated planetary warming and its ocean structure since
571 2006. *Nat. Clim. Change* **5**, 240–245 (2015).
- 572 47. Durack, P. J., Gleckler, P. J., Landerer, F. W. & Taylor, K. E. Quantifying
573 underestimates of long-term upper-ocean warming. *Nat. Clim. Change* **4**, 999–1005
574 (2014).
- 575 48. McDougall, T. J. & Jackett, D. R. The material derivative of neutral density. *J.*
576 *Mar. Res.* **63**, 159–185 (2005).
- 577 49. Häkkinen, S., Rhines, P. B. & Worthen, D. L. Warming of the Global Ocean:
578 Spatial Structure and Water-Mass Trends. *J. Clim.* **29**, 4949–4963 (2016).
- 579 50. Desbruyères, D., McDonagh, E. L., King, B. A. & Thierry, V. Global and Full-
580 Depth Ocean Temperature Trends during the Early Twenty-First Century from Argo
581 and Repeat Hydrography. *J. Clim.* **30**, 1985–1997 (2017).
- 582 51. Iudicone, D. *et al.* Water masses as a unifying framework for understanding the
583 Southern Ocean Carbon Cycle. *Biogeosciences* **8**, 1031–1052 (2011).
- 584 52. Hawkins, E. *et al.* Uncertainties in the timing of unprecedented climates. *Nature*
585 **511**, E3–E5 (2014).
- 586



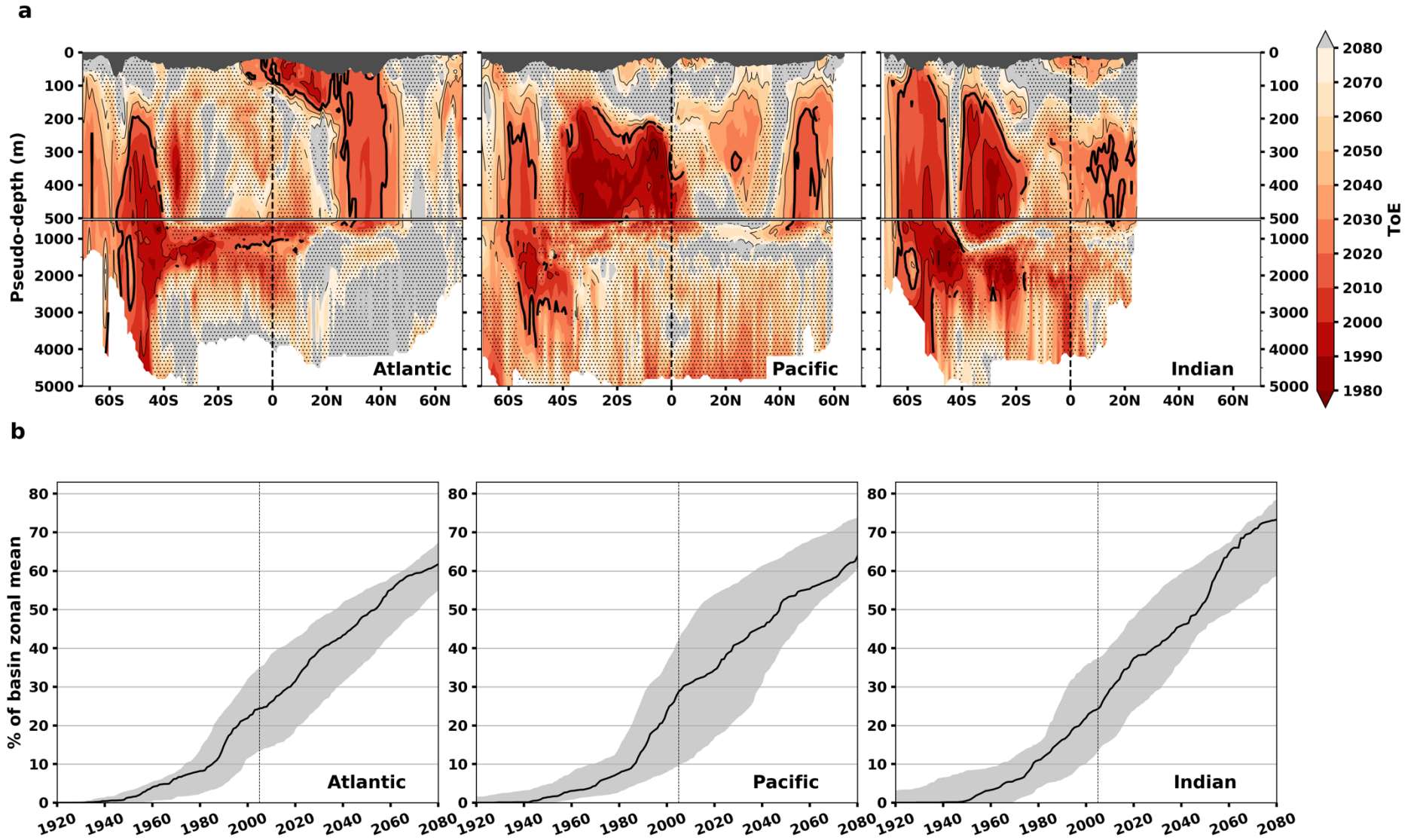
88

89 **Figure 1 Observed and simulated salinity changes between 1950 and 2008, shown in PSS-78/50 years, analysed on density surfaces.** For ease of
 90 reading all figures of this paper are projected back from density to pressure as vertical coordinate (see Methods). (a) From Durack & Wijffels (2010)
 91 observation-based analysis. Contours show isopycnals and stipples where the trend is not significant at the 90% confidence level. (b) From the multi-model
 92 mean historical experiments. Contours show isopycnals and stipples indicate where less than 60% of models agree on the sign of the trend. The changes in
 93 original density coordinate are shown in Supplementary Figure 1. (c) Trend averaged in 9 regions (approximate boxes shown in panel a) for 2 observational
 94 estimates (Durack & Wijffels 2010 - DW10 - and EN4) and for the model distribution (boxes indicate 1st and 3rd quartiles and the median; whiskers indicate
 95 the minimum and maximum outliers). The shading in (c) corresponds to the colour scale of (a) and (b). The exact regions in density space as used for each
 96 observational dataset and model are plotted in Supplementary Figures 1a, 2a and 4 (same coordinates for both observational datasets). The greyed-out regions
 97 at the surface correspond to data trimming above the bowl – see text.



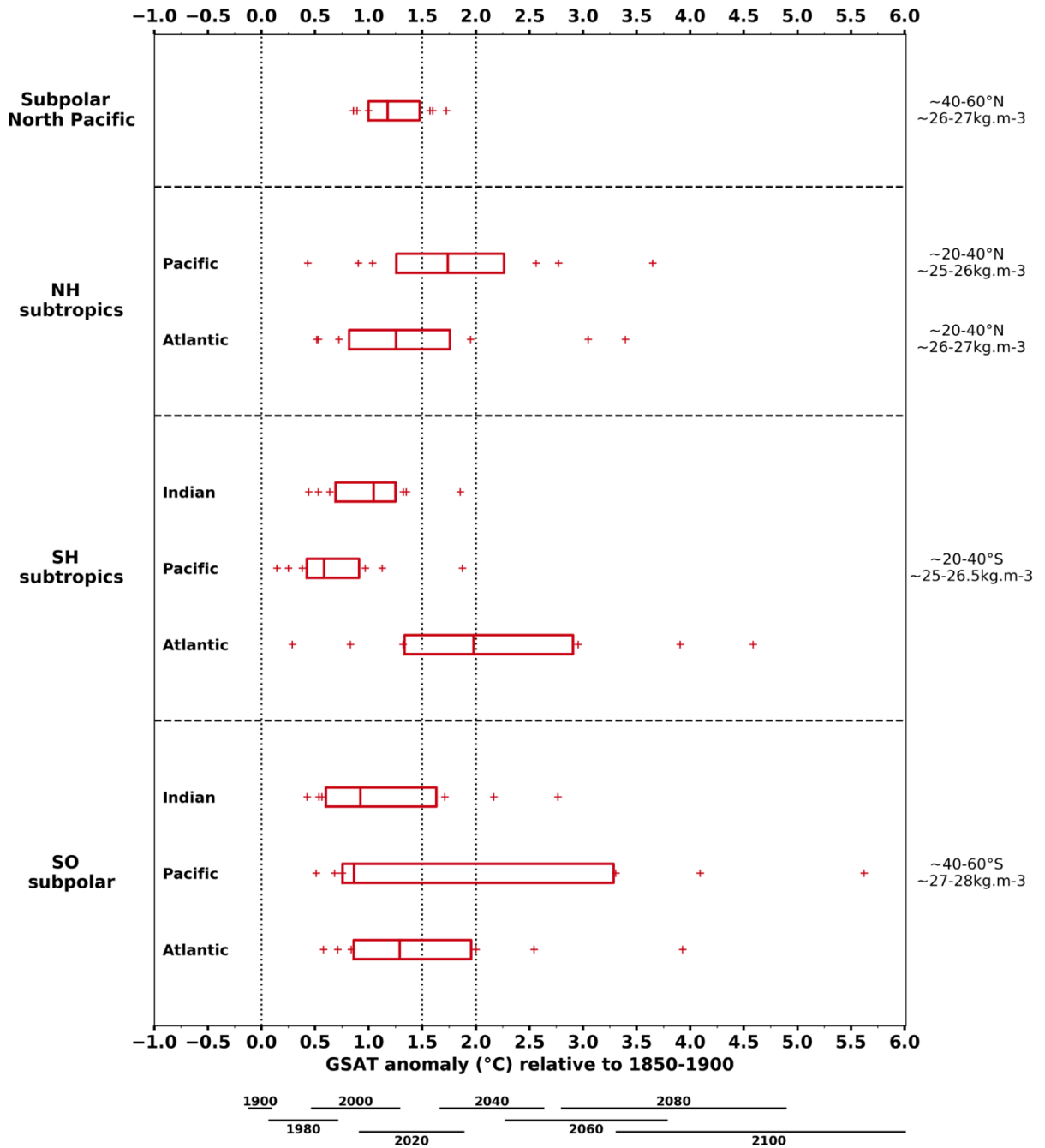
98

99 **Figure 2 Anthropogenic salinity change along density surfaces.** (a) At the end of the 20th century (multi-model mean difference between the last 20 years
 00 – to account for potential decadal variability – of the historical experiment and the historicalNat experiment). (b) At the end of the 21st century (multi-model
 01 mean difference between the last 20 years of the RCP8.5 scenario and the average of the whole historicalNat experiment). Boxes in (b) represent the
 02 approximate regions in which salinity trends are computed in Figure 1c and in which time of emergence is calculated in Figure 4. The same signal as in (b)
 03 is shown in Supplementary Figure 4 for each model in density space with the exact box locations.



04

05 **Figure 3 Time of emergence and percentage of emergence in basin zonal-means.** (a) Multi-model median time of emergence of the anthropogenic salinity
 06 change, calculated for an ensemble of 11 models. Light grey regions mean no emergence of the signal, while stippled regions show where the models don't
 07 agree on the sign of the signal (see Methods). Bold contour is year 2020. (b) Percentage of basin emergence in zonal means under the bowl (see Methods).
 08 The black line is the median, the grey shading is the interquartile range.



609

610
611
612
613
614
615
616
617

Figure 4 Distribution of Global Surface Air Temperature at emergence. Calculated from the anthropogenic salinity signal and noise for each of the 11 models in 9 regions of interest: the Southern Ocean subpolar range, the Southern Hemisphere subtropical range, the Northern Hemisphere subtropical range and the subpolar North Pacific (the exact coordinates for each model are shown in Supplementary Figure 4). Red boxes indicate 1st quartile, median and 3rd quartile. A date reference was added below the warming axis, spanning the range of the historical and RCP8.5 simulations.